

The Narrow Gate: Localized Image-Text Communication in Vision-Language Models

Alessandro Pietro Serra^{1,2*} Francesco Ortu^{1,3*} Emanuele Panizon^{1*} Lucrezia Valeriani^{1,3}
Lorenzo Basile^{1,3} Alessio Ansuini¹ Diego Doimo^{1†} Alberto Cazzaniga^{1†}

¹ AREA Science Park, Trieste, Italy

² SISSA, Trieste, Italy

³ University of Trieste, Trieste, Italy

{diego.doimo, alberto.cazzaniga}@areasciencepark.it

Abstract

*Recent advances in multimodal training have significantly improved the integration of image understanding and generation within a unified model. This study investigates how vision-language models (VLMs) handle image-understanding tasks, specifically focusing on how visual information is processed and transferred to the textual domain. We compare VLMs that generate both images and text with those that output only text, highlighting key differences in information flow. We find that in models with multimodal outputs, image and text embeddings are more separated within the residual stream. Additionally, models vary in how information is exchanged from visual to textual tokens. VLMs that only output text exhibit a distributed communication pattern, where information is exchanged through multiple image tokens. In contrast, models trained for image and text generation rely on a single token that acts as a narrow gate for the visual information. We demonstrate that ablating this single token significantly deteriorates performance on image understanding tasks. Furthermore, modifying this token enables effective steering of the image semantics, showing that targeted, local interventions can reliably control the model's global behavior.*¹

1. Introduction

The rise of foundation models [1] trained on vast amounts of text has transformed natural language processing (NLP),

showing that a single large language model (LLM) [2] can handle many different linguistic tasks [3–5]. The rich set of features encoded in LLM embeddings has been then used as an effective prior knowledge both for text-conditional image generation [6–8] and image understanding [9–13]. Recently, the availability of large open datasets [14, 15] and improved techniques to align text and image embeddings [16] have also enabled the creation of multimodal models that can both understand and generate visual content within a single architecture [17–20]. This unification allows a richer understanding of the visual world, as generative tasks often require insight into the fundamental concepts and relationships within the data [21]. For example, a model that generates images from text descriptions must grasp the semantic content of those images to ensure they faithfully reflect the details and intent of the text [22, 23]. As a result, research has rapidly progressed to integrate multiple modalities into a unified framework with increasingly deeper multimodal fusion. Early approaches used cross-attention modules between modality-specific encoders [17].

However, research by [24] and [25] highlighted the advantage of using a pre-trained LLM backbone combined with lightweight projection layers to align different modalities, significantly enhancing reasoning and understanding capabilities. Further advancements have focused on fine-tuning these LLM backbones [19] and refining early-fusion techniques [16]. More recently, research has shown success in training multimodal-output vision-language models (VLMs) from scratch [20, 26], achieving performance close to VLMs that only output text on visual understanding tasks.

While recent studies have examined the internal mechanisms of unimodal-output VLMs [27–30], little to none is

*Equal contribution

†Equal supervision

¹Code and data: <https://ritareasciencepark.github.io/Narrow-gate>

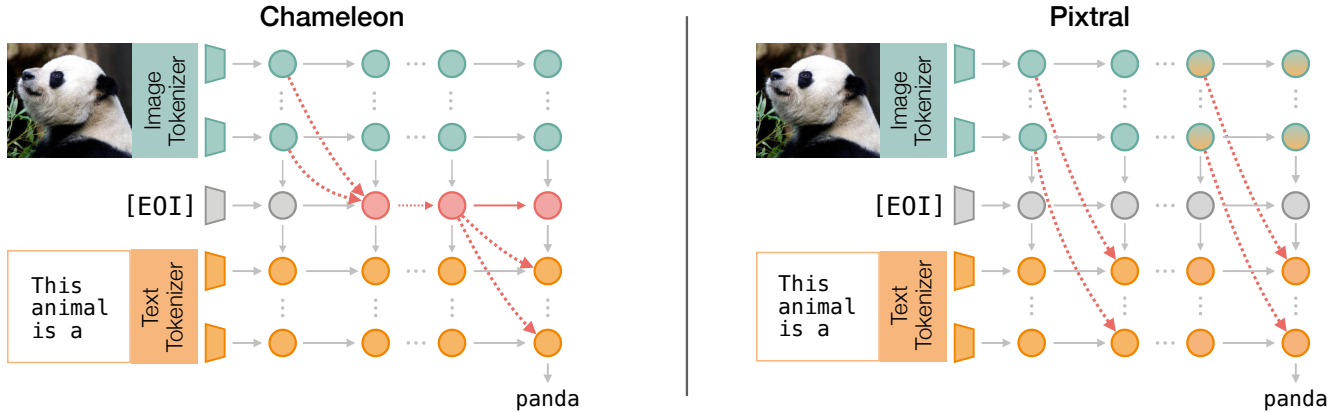


Figure 1. **Image-Text Communication Pathways in VLMs.** Different VLM designs handle information flow between modalities in radically different ways. Chameleon, an early-fusion and multimodal-output model, encodes visual and textual tokens in well separated regions, and knowledge transfer from image to text happens through a *narrow gate*, the end-of-image token [EOI]. On the contrary, Pixtral fuses late-layer visual tokens into the textual domain, as it can output only text, and it features a distributed image-text communication pattern, in which internal image tokens directly communicate with the textual domain.

known about how different modalities interact in the hidden representations of the rich class of multimodal-output models or whether their information processing resembles that of text-only VLMs. In this work, we focus on one of the latest early-fusion multimodal-output VLMs, Chameleon [20], as our primary case study and compare it with Pixtral [13], an unimodal-output VLM, on how they transfer information from the visual domain to the textual domain in various image understanding tasks.

We observe that in Chameleon, the image text representations are largely orthogonal and remain separated in different clusters from input to output, while in Pixtral image and text embeddings tend to mix in late layers (Sec. 4.1). Additionally, in Pixtral, the information flow from image to text is distributed across multiple tokens. In contrast, Chameleon channels the global image information into a single token placed immediately after the image, which we refer to as the *end-of-image token*, denoted by [EOI] (Sec. 4.2). The [EOI] token behaves like a memory token [31] or “narrow gate” through which the image information must pass to guide text generation.

We experimentally demonstrate the crucial role of [EOI], by showing that (1) if we block information flow from [EOI] to textual tokens, model performance dramatically drops across a variety of tasks, including image classification, visual question answering (VQA), and image captioning (see Sec. 4.3); (2) if we edit the information stored in [EOI], we can change the image semantics and its textual description (see Sec. 4.4).

None of these properties hold for Pixtral, where the information between modalities flows through many distributed image tokens specialized for cross-modal communication.

2. Related Works

Special Tokens, Memory Tokens, Registers. The importance of special tokens to store and redistribute global information was emphasized by Burtsev et al. [31]. In their work, they add these special tokens at the beginning of the sequence to serve as memory units accessible through the self-attention mechanism, improving performance on various language processing tasks. In vision transformers, Darcet et al. [32] found that high-norm tokens in low-informative areas of the images are used to store global information while discarding the local one. Adding learnable “register tokens” dedicated to global information processing helped eliminate the high-norm artifacts, improving performance. Similarly, Wen et al. [29] used learnable registers to summarize salient visual information and remove the image tokens altogether, improving the efficiency of vision-language models.

Information Flow in Text-Only VLMs. In text-only VLMs, this summarization is particularly useful since much of the attention to image tokens is concentrated in the initial layers, likely on a few “anchor tokens” [28, 33]. Basu et al. [28] demonstrated with multimodal causal tracing that, in VQA tasks, a subset of strongly attended *late image tokens* in early layers transfer information to the text. However, a later ablation study by Neo et al. [27] showed that important information about objects is often localized in tokens corresponding to the object’s position in the image. Interestingly, they also observed that image tokens — which may have different statistical properties compared to textual tokens [34] — in the deeper layers encode vocabulary words that describe the objects they belong to.

3. Background and Methods

3.1. Model Architectures

A transformer-based VLM [35] first converts a multi-modal input of pixels and text to a sequence t_1, \dots, t_N of N tokens. Each token t_i is then embedded as a vector $x_i^0 \in \mathbb{R}^d$. The input embeddings are then passed through a sequence of L transformer layers, each composed of a multi-head self-attention block followed by an MLP block. Formally, the representation x_i^l of token i at layer l is obtained by:

$$x_i^l = x_i^{l-1} + a_i^l + m_i^l \quad (1)$$

where $a_i^l = a_i^l(x_{i,in}^{l-1})$ and $m_i^l = m_i^l(x_{i,in}^{l-1} + a_i^l)$ are the outputs from the l -th attention and MLP blocks, respectively. We denote with $x_{i,in}^{l-1}$ the input of the attention block, which is then typically normalized and serves as the context for the attention mechanism in a_i^l , to differentiate it from the cumulative residual stream x_i^{l-1} . This distinction will be used in Sec. 4.4. Following the terminology introduced in [36], we denote x_i^l as the *residual stream* of a token t_i at layer l . The attention blocks aggregate information from all positions at the previous layer and consists of \mathcal{H} attention heads, each associated with a lower-triangular weight matrix denoted by A . In most experiments detailed below, prompts follow a consistent format, with an image followed by a textual prompt. This motivates the definition of the following matrix blocks. Let $N_{[\text{EOI}]}$ be the index of the end-of-image token; we can define:

1. $A_{\text{img}} = A_{i,j}$ with $1 \leq i < N_{[\text{EOI}]}$, $0 < j < N_{[\text{EOI}]}$: image self-attention;
2. $A_{\text{text}} = A_{i,j}$ with $N_{[\text{EOI}]} < i \leq N$, $N_{[\text{EOI}]} < j \leq N$: text self-attention;
3. $A_{\text{img} \rightarrow \text{text}} = A_{i,j}$ with $N_{[\text{EOI}]} < i \leq N$, $0 < j < N_{[\text{EOI}]}$: communication between text and image;
4. $A_{\text{target} \rightarrow \text{next}} = A_{i,j}$ with $N_{[\text{EOI}]} < i \leq N$, $j = N_{\text{target}}$: column of A associated with a specific *target token*.

At the last layer, an output probability distribution p is obtained from the final layer representations via a prediction head that projects the representation to the vocabulary space.

Chameleon. We study two Chameleon model variants: a 7B model with 32 layers and hidden dimension 4096, and a 34B model with 48 layers and hidden dimension 8192. Both models use a pre-trained VQ-VAE encoder [37, 38] to transform 512×512 images into sequences of 1024 tokens drawn from a codebook of size 8192. The VLM transformer, based on the Llama-2 architecture [39], is trained end-to-end on an interleaved mixture of all modalities. Chameleon’s vocabulary is split into image and text tokens, with each image sequence framed by a *start-of-image token* ($[\text{SOI}]$) and an *end-of-image token* ($[\text{EOI}]$) boundaries, allowing unified handling of visual and textual data.

Pixtral. Pixtral is a 12B-parameter model with 40 layers and a hidden dimension of 5120, utilizing a vision transformer encoder that natively supports variable image sizes. Images are tokenized and embedded using a vision transformer, which processes patches of 16×16 pixels. The resulting tokens are interleaved with *end-of-line tokens* ($[\text{EOL}]$) between rows and an *end-of-image token* ($[\text{EOI}]$) at the end, enabling Pixtral to handle images with diverse resolutions and aspect ratios efficiently. The vision transformer has 400 million parameters and was trained from scratch on images. Starting from the backbone Mistral Nemo 12B [40], a decoder-only language model pre-trained on large text corpus, Pixtral was fine-tuned to predict the next textual token on interleaved image and text input data.

3.2. Analytical Tools

Quantification of Cross-Modal Attention. We construct a metric that quantifies the average attention that all the text tokens give to a token at position j within the image part of the prompt, which we assume to span the first $N_{[\text{EOI}]}$ tokens. Formally, we define the (relative) *cross-modal attention* f_j^l as

$$f_j^l = \frac{1}{C} \frac{1}{|\mathcal{H}|} \sum_{h \in \mathcal{H}} \sum_{i > N_{[\text{EOI}]}} A_{(i,j)}^{l,h} \quad (2)$$

Where $j = 0, 1, \dots, N_{[\text{EOI}]}$, l, h identify, respectively, the layer and head, and $A_{i,j}$ denotes the attention from the i^{th} to the j^{th} token. C is a normalization factor such that $\sum_{j \leq N_{[\text{EOI}]}} f_j^l = 1$. This metric, in general, aggregates on the tokens’ *position* in the prompt and not on their identity; the two coincide only for the special tokens.

Neighborhood Overlap. Given a residual representation $\{x_i^l\}$ of n data points at layer l we denote by $\mathcal{N}^l(i)$ the set of k -nearest neighbors of the i -th vector x_i^l . Let us now consider an arbitrary labeling $\{y_i\}$ of the same data, referred to as its ground truth. We assess how well the geometric arrangement of the representations $\{x_i^l\}$ aligns with the labels $\{y_i\}$ by employing the neighborhood overlap (NO) quantity introduced by [41]. Intuitively, the NO, represented as $\chi^{l,gt}$, is the average fraction of k -nearest neighbors for each representation vector that share the same label, calculated across the entire dataset. More formally, defining a ground truth adjacency matrix as follows: $A_{ij}^{gt} = 1$ if $y_i = y_j$ and 0 otherwise, the NO of $\{x_i^l\}$ with the labeling $\{y_i\}$ can be written as:

$$\chi^{l,gt} = \frac{1}{n} \sum_i \frac{1}{k} \sum_{j \in \mathcal{N}^l(i)} A_{ij}^{gt} \quad (3)$$

In this work, we will use NO as a *semantic probe* to quantify the information content in the residual stream.

Attention Knockout. We use the *attention knockout* technique introduced in [42], which selectively blocks attention between certain tokens at selected model layers. Given a set of source tokens \mathcal{S} and a set of target tokens \mathcal{T} , we prevent the target tokens from attending to the source tokens by zeroing out the corresponding entries, $\alpha_{(i,j)}$, in the attention matrix, where $i \in \mathcal{S}$ and $j \in \mathcal{T}$. This intervention is applied across all attention heads within the specified layers.

Activation Patching. To evaluate the effect of specific model components on predictions, we adopt the *activation patching* technique, widely used in prior works [43, 44]. This approach involves two forward passes on two different inputs: first, we collect target activations \hat{x}_i^l ($\hat{x}_{i,\text{in}}^l$) at a given position i and layer l from the first input. Then, while processing a second input, we replace the base activation x_i^l ($x_{i,\text{in}}^l$) with the target activation \hat{x}_i^l ($\hat{x}_{i,\text{in}}^l$). By measuring the impact on the model’s final prediction, we quantify the influence of different model components on its generative process. We quantify the effect of these interventions by measuring the similarity between the output probability distribution of the target (p_{target}) inputs and the probability distribution of the base inputs after patching ($q_{\text{base}}^{\text{patched}}$). The similarity measure is calculated using a variant of the Jaccard index [45], defined as:

$$\text{Similarity}(q_{\text{base}}^{\text{patched}}, p_{\text{target}}) = \sum_i \min(q_i, p_i) \quad (4)$$

This score quantitatively measures how closely the modified model output aligns with the target distribution after activation patching. The score is 1 if p and q are identical and 0 if their supports are fully disjoint.

3.3. Experimental Setup

Implementation Details. Detailed experimental settings, including dataset composition, prompt usage, and pair selection criteria, are provided in Supp. Sec. 8.

Reproducibility. To perform our experiments we employed HuggingFace implementations of Chameleon models [46, 47] and Pixtral-12B [48]. All the experiments on Chameleon-7B and Pixtral-12B were executed on a single NVIDIA A100 GPU equipped with 40GB VRAM, while the experiments on Chameleon-34B were performed using two A100 with 40GB VRAM each.

4. Results

4.1. Modality Gap in Multimodal-Output VLMs

Multimodal-output VLMs, such as models in the Chameleon family, can generate image and text tokens within the same

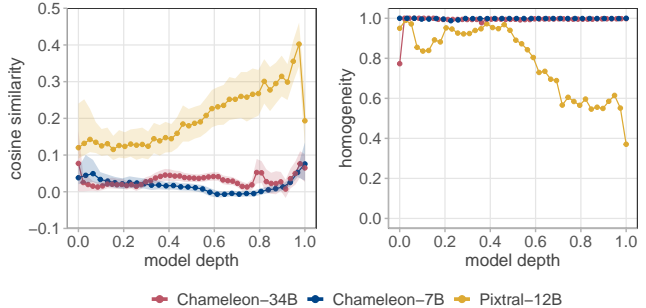


Figure 2. **Modality Gap in VLMs.** (left) Cosine similarity between text and image token embeddings as a function of model depth reflects the orthogonality of modalities in Chameleon models. Points represent median cosine similarity, with shaded areas indicating the interquartile range. (right) Homogeneity score of token clusters generated via Advanced Density Peaks with respect to their original modality.

transformer backbone. Thus, they leverage shared parameters to perform the next token prediction task on all modalities in a unified representation space. In contrast, unimodal-output VLMs, such as Pixtral, generate textual tokens using image tokens only as contextual information. Although both types of VLMs use a joint residual stream for both image and text tokens, the role of each modality in the generation process differs significantly. This observation leads us to investigate whether models that generate both modalities favor the emergence of modality-specific regions of the residual stream space that separate image and text representations.

To address this question, we randomly select 10,000 image-caption pairs from the Flickr30k dataset [49]. To consider the effect of conditional generation in both modalities, we construct 10,000 prompts with an image followed by text and 10,000 prompts with reverse ordering. We then perform a forward pass through the model, storing hidden representations in the residual stream for each modality across all layers. For any image-text pair, we extract the hidden representations at a randomly chosen *text token position*. When the order is reversed (text before image), we focus on the representations at a randomly chosen *image token position*. Details on prompt construction are provided in Supp. Sec. 8.

We compare the geometric organization of the different modalities by measuring the median cosine similarity between representations of image and text tokens in hidden layers. Fig. 2 (left) shows the cosine similarity for Chameleon-7B (blue), Chameleon-34B (red), and Pixtral-12B (yellow). In Chameleon models, the representative vectors of image and text tokens remain nearly orthogonal across the hidden layers, with median cosine similarity values consistently below 0.1. In Pixtral, cosine similarity values are higher, beginning at 0.2 at the network’s initial layers and progressively rising to 0.4 towards the final layers. This upward trend in cosine similarity between image and text represen-

tations suggests that the two modalities increasingly mix in the later layers. To further investigate the degree of mixture of modalities in Chameleon and Pixtral, we apply the Advanced Density Peaks clustering method [50] (see Appendix, Supp. Sec. 7 for a brief introduction) and analyze the composition of each cluster. Fig. 2 (right) shows the homogeneity score [51] of the clusters that measures how the clustering of tokens aligns with their modality. In Chameleon models (red and blue profiles), the homogeneity score is always 1, meaning each cluster contains a single modality embedding. In contrast, in Pixtral, the homogeneity score decreases from almost 1 to approximately 0.5 in the second part of the network, indicating a tendency of the text and image embeddings to mix.

We conclude that textual and visual representation spaces are largely separated in Chameleon models. This brings forth the problem of finding how and where communication between the two modalities is performed.

4.2. Analysis of Cross-Modal Attention

As shown in Sec. 4.1, hidden representations of visual and textual tokens are mixed in late layers of text-output models, while they pertain to well-separated regions of the residual stream in multimodal-output models. Despite this structural difference, both model types achieve high performance on image understanding tasks, which suggests that attention maps effectively transfer semantic information from the image to the text. To achieve this, the attention matrices of Chameleon models play another important role: while sharing information among modalities they need to bridge the modality gap. These observations lead us to define two fundamental features for tokens to handle efficient cross-modal communication: *i)* having a large weight in the text-image attention and *ii)* having a rich semantic knowledge of the image. In the following, we investigate whether the Chameleon and Pixtral models have tokens that satisfy both requirements, thus being candidates for the role of *gate* of communication between modalities.

Cross-Modal Attention Patterns. To quantify the role of each token in image-to-text semantic communication, we begin by constructing 10,000 prompts of images followed by text, of the form “`<image> This animal is a ..`”. We randomly select 100 images per class for 100 animal classes within the ImageNet dataset [52]. The sentence was chosen to guide the model towards generating a class-relevant response. For the full list of chosen classes, refer to Supp. Sec. 8.

Fig. 3 illustrates the relative text-on-image attention, as defined in Sec. 3.2, at different token positions. We single out tokens with an average value larger than 1%. The remaining tokens are aggregated as either *internal image* or *end-of-line* ([EOL]), depending on their nature. In the

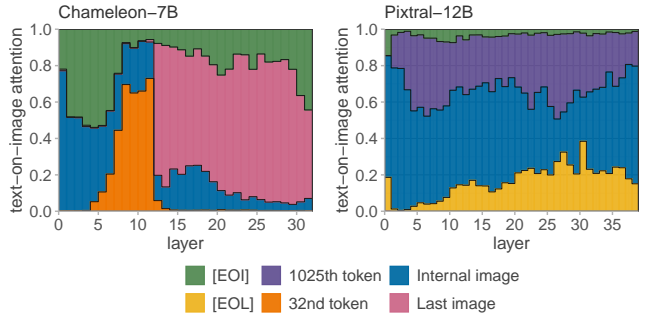


Figure 3. **Cross-Modal Attention Contributions of Tokens.** Contribution of different image token positions to the total text-on-image attention across layers in Chameleon-7B (left) and Pixtral-12B (right), computed on ImageNet data. Tokens with an average contribution larger than 1% are shown individually. The remaining tokens are aggregated as “internal image” or [EOL]s depending on their type.

left panel, we show the distribution for Chameleon-7B. The special [EOI] token captures over 40% of the cross-modal attention in layers 2 to 6, with the remaining attention distributed among the other 1024 image tokens. In the middle layers, the [EOI] token maintains a contribution between 8% and 12%, which increases again to over 37% in the final two layers. The last token of the image sequence also shows significant attention, contributing between 66% and 86% in the middle and final layers. Notably, the 32nd image token dominates attention between layers 7 and 11, peaking at over 60% between layers 8 and 11. The contribution from the remaining image tokens stays below 28% from layer 8 onward, progressively decreasing to less than 10% after layer 26. Chameleon-34B, as shown in Supp. Sec. 9, exhibits a similar contribution to the attention from the [EOI] token, while also distributing attention across other tokens. In the right panel, we present the distribution of average attention among tokens in Pixtral-12B. The 1025th image token contributes between 17% and 46% of the total attention from layer 4 to the end of the model. The [EOL] tokens account for approximately 20% of the attention between layers 20 and 35, with the remaining attention distributed across the other image tokens.

Neighborhood Overlap of Embeddings. The analysis of total attention contributions reveals that a few localized tokens, such as the [EOI] and last image tokens in Chameleon-7B, or the [EOL], 32nd and 1025th image tokens in Pixtral-12B, are strongly attended by text tokens, significantly shaping image-to-text communication. To investigate whether these tokens contain semantic visual information, we extract their hidden representations for all image inputs in our dataset across all layers. Then, we compute the neighborhood overlap between these representations and the Im-

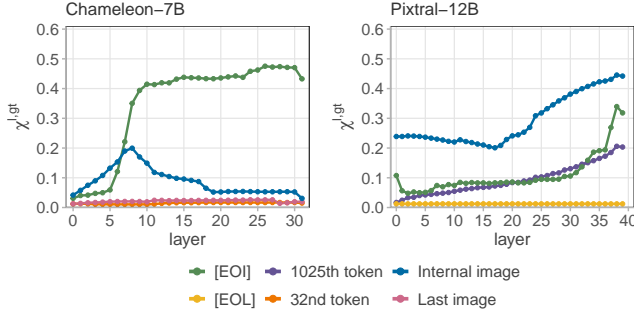


Figure 4. **Localization of Visual Semantic Information.** Neighborhood overlap between selected image tokens and ImageNet labels for Chameleon-7B (left) and Pixtral-12B (right). The blue curves are obtained by averaging over all internal image tokens excluding the 32nd token for Chameleon and the 1025th for Pixtral, the yellow one by averaging over end-of-line ([EOL]) tokens.

geNet class labels of the corresponding image for each layer, averaging across token positions when considering multiple tokens.

Fig. 4 (left) shows that, in Chameleon-7B, the representation of the [EOI] token starts with a $\chi^{l,gt}$ near 0 in the first five layers and then rapidly increases, exceeding 0.4 from layer 9 to the end of the network. In contrast, the representations at the 32nd and last image token remain consistently near 0 across all layers, suggesting that these positions do not contribute to encoding meaningful visual information about the image. The representations of the remaining image tokens increase from a $\chi^{l,gt}$ of 0 in the initial layers to approximately 0.2 at the 8th layer but then gradually decrease, falling below 0.1 from layer 15 onward. These findings indicate that, in Chameleon-7B, most image token positions contribute to encoding visual information in the early layers, but beyond the 8th layer, only the representation at the [EOI] token position retains meaningful information about the image. For Chameleon-34B, we observe similar results: the hidden representations of the [EOI] token achieve $\chi^{l,gt} > 0.4$ after layer 16, while the other visual token representations have overlap below 0.25 throughout the network. The complete results for Chameleon-34B are presented in Fig. A1 in Supp. Sec. 9. In contrast, as shown in Fig. 4 (right), in Pixtral-12B, the representations of all image tokens, except those at the end-of-lines ([EOL]), consistently increase their $\chi^{l,gt}$ with ImageNet class representations across layers. Notably, the internal image token representations exhibit the highest $\chi^{l,gt}$ across all layers, starting from a relatively high value of 0.24 at layer 0 and progressively increasing to 0.44 by the final layer. This initial overlap is consistent with the fact that the visual encoder of Pixtral-12B already possesses meaningful visual features even at the earliest stages of the model.

The results above show that in the Chameleon models

the [EOI] token is responsible for a large portion of cross-modal attention and contains the highest semantic information regarding the image. This makes it a suitable candidate for being a *narrow gate* of communication. Conversely, in Pixtral the semantic content is spread on the whole image representation, thus suggesting that the model uses a much wider gate of communication distributed across large portions of the image.

4.3. Ablation Experiments: The Effect of Localized Communication on Downstream Tasks

Building on the previous analysis, where we identified the token positions responsible for encoding visual features and those receiving the strongest attention during image-to-text communication, we now investigate their impact on the flow of information through the network. Specifically, we analyze how the presence of these features influences the representations in the final layers, particularly at the last token position, which plays a critical role in generating the model’s output.

Measuring the Effect of the Image-to-Text Communication Through Attention Knockout. To perform this analysis, we use the same dataset and prompt structure (“{image} This animal is a __”) described in Sec. 4.2. We now compute the neighborhood overlap ($\chi^{out,gt}$) at the last layer and last text token position after applying *attention knockout*. As detailed in Sec. 3.2, we block communication between [EOI] and text tokens, as well as between the residual streams of all visual and text tokens, by zeroing out respectively $A_{[EOI] \rightarrow \text{text}}$ and $A_{\text{img} \rightarrow \text{text}}$ as described in Sec. 3.1. The knockout is performed progressively, ablating communication from layer l to the end of the network, with l starting at the last layer and decreasing in steps of 4. For each window of ablated layers, we compute $\chi^{out,gt}$ to evaluate the effect of the ablation on the final representation.

Fig. 5 presents the results for all three models studied, showing the value of $\chi^{out,gt}$ as a function of the number of layers ablated starting from the end. In both Chameleon-7B (left) and Chameleon-34B (center), enlarging the ablation window for the communication between [EOI] and text leads to a progressive decrease in the value of $\chi^{out,gt}$. The baseline value without ablation starts at 0.46 for Chameleon-7B and 0.43 for Chameleon-34B, decreasing to near 0 when communication is blocked across all layers. In contrast, when ablating the communication between all residual streams at image positions and the text, the value of $\chi^{out,gt}$ at the last token representation remains constant at the baseline value, regardless of the size of the ablation window. These results show that visual information is not directly transmitted between the residual representations of image tokens and those of text tokens; instead, it flows through [EOI]. In contrast, Fig. 5 (right) shows the opposite behavior in Pixtral-12B. The value of $\chi^{out,gt}$ remains constant at

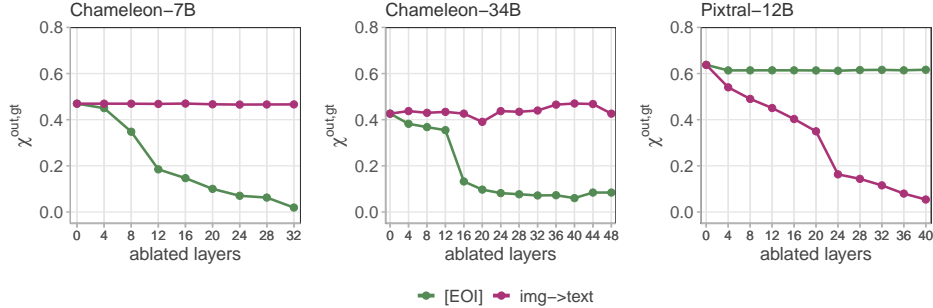


Figure 5. **Effect of Progressive Attention Knockout.** Neighborhood overlap between model final layer representations at the last text token positions and ImageNet classes when applying attention knockout. Prompts follow the format: $\langle \text{image} \rangle$ This animal is a $_$ ” (see Sec. 4.2). Communication from the [EOI] token position (green) to the text or from all image token positions (magenta) to the text is ablated across an increasing number of layers, starting from the last.

Model	Ablation	VQAv2	Flickr	MS-COCO	ImageNet
Chameleon-7B	-	0.51	0.23	0.35	0.46
	[EOI]	0.25	0.04	0.03	0.01
	img \rightarrow text	0.40	0.13	0.21	0.47
	random	0.51	0.21	0.31	0.46
Chameleon-34B	-	0.59	0.38	0.42	0.43
	[EOI]	0.39	0.02	0.02	0.04
	img \rightarrow text	0.50	0.25	0.28	0.42
	random	0.58	0.34	0.38	0.42
Pixtral	-	0.79	0.51	0.60	0.63
	[EOI]	0.77	0.53	0.58	0.61
	img \rightarrow text	0.37	0.00	0.01	0.06
	random	0.77	0.46	0.55	0.61

Table 1. **Effect of Attention Knockout on Image Understanding Tasks.** Performance of Chameleon (7B and 34B) and Pixtral models on visual question answering (VQAv2), image captioning (Flickr-30k and MS-COCO), and image classification (ImageNet) under different attention ablation settings. The [EOI] ablation condition removes communication from the End of Image ([EOI]) token to text tokens. The “img \rightarrow text” ablation blocks communication from all image tokens to text tokens while preserving communication from the [EOI] token to text. The random baseline represents the average performance after ablating 10 randomly selected image tokens, repeated 10 times (standard deviation < 0.02).

the baseline level of 0.6 when ablating the communication between the residual stream at the [EOI] token position and the text. However, it decreases to 0 progressively, layer by layer, when ablating the communication from the residual streams of internal image tokens to text tokens.

Quantifying the Role of Image-Text Communication for Visual Understanding Tasks. Next, we evaluate how applying *attention knockout* to block communication between specific token positions and the text affects the general performance of the models on more complex visual understanding tasks. Specifically, we evaluate the models on three standard benchmarks: VQAv2 [53] for visual question answering, Flickr30k [49] and MS-COCO [54] for image captioning.

Details on the evaluation metrics for each task are provided in Supp. Sec. 8. To conduct this analysis, we first randomly sample 2000 data points from each dataset and establish performance baselines for each model. We then apply attention knockout to block communication from the residual streams of the [EOI] token and from the all image tokens. We also report the attention knockout of 10 randomly selected tokens within the image as a baseline.

The results are summarized in Tab. 1. For comparison, we also report the value of $\chi^{out,gt}$ computed in the last layer at the last textual token using the same ImageNet-based dataset described above. Further results on the impact of ablation at other special token positions, such as the last image token for the Chameleon models and the 1025th image token and [EOL] for Pixtral-12B, are provided in Supp. Sec. 10.

In Chameleon models, we observe a significant drop in performance across all four tasks when the communication between the residual stream at the [EOI] token position and the text is blocked. On VQAv2, the performance of Chameleon-7B decreases from 0.51 to 0.25, while in Chameleon-34B it drops from 0.59 to 0.39. The decline is even more pronounced in captioning tasks: Chameleon-7B falls from a baseline of 0.23 on Flickr30k to 0.04, while Chameleon-34B drops from 0.38 to 0.02. On MS-COCO, both Chameleon-7B and Chameleon-34B experience more than a 90% reduction in baseline performance. These results align with the corresponding drop in the value of $\chi^{out,gt}$, further confirming that blocking communication at the [EOI] token position prevents semantic information from flowing from the image to the text. In the complementary experiment, where communication between modalities occurs only through the token [EOI] by zeroing out $A_{img \rightarrow text}$, we observe only a small drop in performance. For example, on VQAv2, Chameleon-7B achieves a performance above 0.40, and Chameleon-34B remains above 0.50, compared to baselines of 0.51 and 0.59, respectively. Similar patterns are observed across the remaining tasks, further

confirming that the majority of the communication between the 1024 image tokens and the text is mediated through the $[\text{EOI}]$ token. Finally, blocking communication at ten randomly selected image token positions does not significantly harm performance.

For Pixtral-12B, the results vary according to the ablation scenario. While no significant performance drop is observed when blocking communication at the $[\text{EOI}]$ token or in random token ablations (e.g., VQAv2 performance remains above 0.77 compared to a baseline of 0.79), a sharp difference emerges when communication from image tokens to text is blocked entirely. Under this condition, Pixtral-12B performance falls, reaching 0.00 on Flickr30k and 0.01 on MS-COCO, compared to baselines of 0.51 and 0.60, respectively. These findings indicate that the Pixtral-12B model does not rely on specific token positions to solve visual understanding tasks.

Overall, the results of our ablation experiments confirm that the cross-modal communication in the Chameleon models flows mainly through a *single* token, the special $[\text{EOI}]$ token. On the contrary, in Pixtral-12B such communication happens in a distributed fashion through the image itself, meaning that it cannot be disrupted with a local intervention.

4.4. Steering Image Understanding Through Activation Patching

So far, we have shown that in Chameleon models, $[\text{EOI}]$ encodes global information about the image (see Sec. 4.2), and it is the main communication gateway to the text (see Sec. 4.3). In this section, we show that the localized nature of cross-modal communication in Chameleon-7B and Chameleon-34B allows a targeted editing of image semantics. To do so, we perform a patching experiment selecting 20 animal classes from the ImageNet dataset, sampling 100 images from each class. We group the classes into ten pairs and construct the experiment as follows: i) we collect the $[\text{EOI}]$ representation at each layer l for the examples of one class of the pair, the target class $[\text{EOI}]^{l,\text{target}}$; ii) we classify images of the other class of the pair, the base class, in which $[\text{EOI}]^{l,\text{base}}$ is replaced by $[\text{EOI}]^{l,\text{target}}$ at selected layers. The details on the prompt used and the selected classes are in Supp. Sec. 8.

In the first experiment, we set $[\text{EOI}]^{l^*,\text{base}}$ to $[\text{EOI}]^{l^*,\text{target}}$ in the residual stream. With this intervention, we modify the representation of $[\text{EOI}]$ of the base class for all the layers $l > l^*$ through the residual connections. The left panel of Fig. 6 shows the effect of this patching in Chameleon-7B (blue profile) and Chameleon-34B (red profile). On the y -axis, we plot the similarity between the probability distribution of the base class and the target class defined in Eq. (4). The horizontal dashed line represents the baseline similarity of the output distribu-

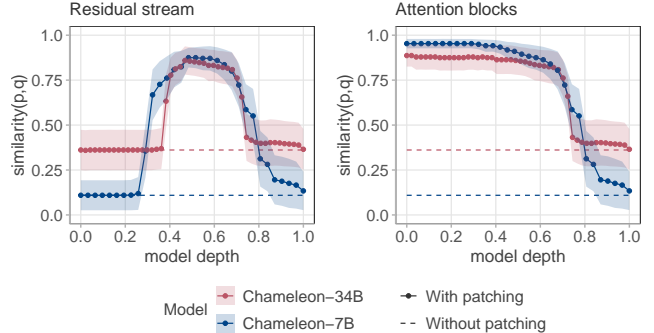


Figure 6. **Impact of Activation Patching at $[\text{EOI}]$ in Chameleon Models.** Similarity (according to Eq. (4)) between the probability distributions over the vocabulary for the target input and the base input across different layers. **(left)** Impact of patching the *residual stream* at each layer. **(right)** Impact of cumulative patching of the sole input of *attention blocks*, starting from the point indicated on the x-axis through the end of the model.

tion between the two classes, averaged over the ten pairs. This baseline is larger than zero because of the intrinsic similarity between animals of the two classes. The full profiles represent the effect of the patching of $[\text{EOI}]^{l,\text{target}}$ on the base class. In the initial layers, editing $[\text{EOI}]$ has no significant effect on $\text{Similarity}(q_{\text{base}}^{\text{patched}}, p_{\text{target}})$ since the information from the image has not reached $[\text{EOI}]$ yet. Indeed, in Sec. 4.2, Fig. 4 (left), we saw that in Chameleon-7B, $\chi^{l,\text{gt}}$ of $[\text{EOI}]$ grows between layers 5 and 10, which corresponds to 0.16 to 0.33 of relative depth. Consistently, the patching of $[\text{EOI}]^{l^*,\text{target}}$ becomes more effective after a relative depth of 0.3 (see the blue profile of Fig. 6 (left)), and it reaches a peak of 0.86 at layer 15 (0.5 of relative depth). Patching $[\text{EOI}]^{l,\text{target}}$ into $[\text{EOI}]^{l,\text{base}}$ alone changes the class prediction from base to target 75% of the times (see Supp. Sec. 11). After 0.7 of relative depth, $\text{Similarity}(q_{\text{base}}^{\text{patched}}, p_{\text{target}})$ decreases rapidly, returning to near-baseline levels at the last layer. This decrease suggests that most image information is passed to the last token position in the middle layers. A similar picture holds for Chameleon-34B (red profile).

In the second experiment, we update $[\text{EOI}]^{l,\text{base}}$ for all layers $l > l^*$ using the attention constructed with $[\text{EOI}]^{l,\text{target}}$. In practice, we set $x_{[\text{EOI}],\text{in}}^{l-1} = [\text{EOI}]^{l-1,\text{target}}$ (see Sec. 3.1 for details on $x_{i,\text{in}}^{l-1}$). In Fig. 6 (right), we show the results for cumulative attention patching in blue for Chameleon-7B and red for Chameleon-34B. The value at layer 0, around 0.95 for Chameleon-7B and 0.87 for Chameleon-34B, represents a condition in which the textual tokens attend to $[\text{EOI}]^{\text{target}}$ instead of $[\text{EOI}]^{\text{base}}$. Even with the textual tokens attending to the image *base* class, the information communicated by $[\text{EOI}]^{\text{target}}$ alone can completely replace the original image semantics. This effect persists until a relative depth of 0.6 when the seman-

tics from $[EOI]^{target}$ has already been “written” into the textual tokens, maintaining a similarity to the target distribution above 0.75. The drop in similarity between relative depths 0.6 and 0.8 indicates that the attention blocks transfer information from $[EOI]^{target}$ to the textual tokens for up to 80% of the model depth (corresponding to layer 26 and 34 for Chameleon-7B and Chameleon-34B respectively). Beyond this depth, further modification in the attention blocks has little impact, as similarity levels drop to near baseline for both models. This suggests that these final layers have a limited role in encoding semantics, as the necessary information has already been communicated to the textual tokens in earlier layers.

5. Conclusion

In this study, we compare the information flow pathways in Chameleon, a multimodal-output VLM, with Pixtral, an unimodal-output VLM. In Chameleon, we find that the cross-modal communication is localized and flows through $[EOI]$, while, consistently with previous studies [27, 28], we find that in unimodal-output models, the decision process is distributed across many visual tokens. The localized communication through $[EOI]$ simplifies the process of tracking how visual information is translated into text, offering clearer insights into the decision-making process of these models. At the same time, the ability to steer image semantics by only editing a single $[EOI]$ token raises opportunities and concerns. It opens possibilities for targeted image editing and content creation but also highlights potential vulnerabilities to manipulation and bias. Future research should focus on understanding whether this communication mechanism extends to other multimodal output VLMs and developing techniques to mitigate the potential risks associated with the controllability of the narrow gate.

6. Acknowledgments

The authors acknowledge the AREA Science Park supercomputing platform ORFEO made available for conducting the research reported in this paper and the technical support of the Laboratory of Data Engineering staff. Alessandro Pietro Serra, Francesco Ortu, Emanuele Panizon, Lorenzo Basile, Alessio Ansuini, Diego Doimo and Alberto Cazzaniga were supported by the project “Supporto alla diagnosi di malattie rare tramite l’intelligenza artificiale” CUP: F53C22001770002 and “Valutazione automatica delle immagini diagnostiche tramite l’intelligenza artificiale”, CUP: F53C22001780002. Alessio Ansuini and Alberto Cazzaniga were supported by the European Union – NextGenerationEU within the project PNRR “PRP@CERIC” IR0000028 - Mission 4 Component 2 Investment 3.1 Action 3.1.1. Lucrezia Valeriani was supported by the project “QuB - Quantum Behavior in Biological Function” CUP: J95F21002820001.

References

- [1] Rishi Bommasani, Drew A. Hudson, Ehsan Adeli, Russ Altman, Simran Arora, Sydney von Arx, Michael S. Bernstein, Jeannette Bohg, Antoine Bosselut, Emma Brunskill, Erik Brynjolfsson, S. Buch, Dallas Card, Rodrigo Castellon, Niladri S. Chatterji, Annie S. Chen, Kathleen A. Creel, Jared Davis, Dora Demszky, Chris Donahue, Moussa Doumbouya, Esin Durmus, Stefano Ermon, John Etchemendy, Kawin Ethayarajh, Li Fei-Fei, Chelsea Finn, Trevor Gale, Lauren E. Gillespie, Karan Goel, Noah D. Goodman, Shelby Grossman, Neel Guha, Tatsunori Hashimoto, Peter Henderon, John Hewitt, Daniel E. Ho, Jenny Hong, Kyle Hsu, Jing Huang, Thomas F. Icard, Saahil Jain, Dan Jurafsky, Pratyusha Kalluri, Siddharth Karamcheti, Geoff Keeling, Fereshte Khani, O. Khattab, Pang Wei Koh, Mark S. Krass, Ranjay Krishna, Rohith Kuditipudi, Ananya Kumar, Faisal Ladhak, Mina Lee, Tony Lee, Jure Leskovec, Isabelle Levent, Xiang Lisa Li, Xuechen Li, Tengyu Ma, Ali Malik, Christopher D. Manning, Suvir P. Mirchandani, Eric Mitchell, Zanele Muniyikwa, Suraj Nair, Avani Narayan, Deepak Narayanan, Benjamin Newman, Allen Nie, Juan Carlos Niebles, Hamed Nilforoshan, J. F. Nyarko, Giray Ogut, Laurel Orr, Isabel Papadimitriou, Joon Sung Park, Chris Piech, Eva Portelance, Christopher Potts, Aditi Raghunathan, Robert Reich, Hongyu Ren, Frieda Rong, Yusuf H. Roohani, Camilo Ruiz, Jack Ryan, Christopher R’e, Dorsa Sadigh, Shiori Sagawa, Keshav Santhanam, Andy Shih, Krishna Parasuram Srinivasan, Alex Tamkin, Rohan Taori, Armin W. Thomas, Florian Tramèr, Rose E. Wang, William Wang, Bohan Wu, Jiajun Wu, Yuhuai Wu, Sang Michael Xie, Michihiro Yasunaga, Jiaxuan You, Matei A. Zaharia, Michael Zhang, Tianyi Zhang, Xikun Zhang, Yuhui Zhang, Lucia Zheng, Kaitlyn Zhou, and Percy Liang. On the opportunities and risks of foundation models. *ArXiv*, 2021. 1
- [2] Tom Brown, Benjamin Mann, Nick Ryder, Melanie Subbiah, Jared D Kaplan, Prafulla Dhariwal, Arvind Neelakantan, Pranav Shyam, Girish Sastry, Amanda Askell, Sandhini Agarwal, Ariel Herbert-Voss, Gretchen Krueger, Tom Henighan, Rewon Child, Aditya Ramesh, Daniel Ziegler, Jeffrey Wu, Clemens Winter, Chris Hesse, Mark Chen, Eric Sigler, Mateusz Litwin, Scott Gray, Benjamin Chess, Jack Clark, Christopher Berner, Sam McCandlish, Alec Radford, Ilya Sutskever, and Dario Amodei. Language models are few-shot learners. In H. Larochelle, M. Ranzato, R. Hadsell, M.F. Balcan, and H. Lin, editors, *Advances in Neural Information Processing Systems*, volume 33, pages 1877–1901. Curran Associates, Inc., 2020. 1
- [3] Jonathan Berant, Andrew Chou, Roy Frostig, and Percy Liang. Semantic parsing on Freebase from question-answer pairs. In David Yarowsky, Timothy Baldwin, Anna Korhonen, Karen Livescu, and Steven Bethard, editors, *Proceedings of the 2013 Conference on Empirical Methods in Natural Language Processing*, pages 1533–1544, Seattle, Washington, USA, October 2013. Association for Computational Linguistics. 1
- [4] Dzmitry Bahdanau, Kyunghyun Cho, and Yoshua Bengio. Neural machine translation by jointly learning to align and translate, 2016.

- [5] Mehdi Allahyari, Seyedamin Pouriye, Mehdi Assefi, Saeid Safaei, Elizabeth D. Trippe, Juan B. Gutierrez, and Krys Kochut. Text summarization techniques: A brief survey, 2017. 1
- [6] Aditya Ramesh, Mikhail Pavlov, Gabriel Goh, Scott Gray, Chelsea Voss, Alec Radford, Mark Chen, and Ilya Sutskever. Zero-shot text-to-image generation, 2021. 1
- [7] Chitwan Saharia, William Chan, Saurabh Saxena, Lala Li, Jay Whang, Emily L Denton, Kamyar Ghasemipour, Raphael Gontijo Lopes, Burcu Karagol Ayan, Tim Salimans, Jonathan Ho, David J Fleet, and Mohammad Norouzi. Photorealistic text-to-image diffusion models with deep language understanding. In S. Koyejo, S. Mohamed, A. Agarwal, D. Belgrave, K. Cho, and A. Oh, editors, *Advances in Neural Information Processing Systems*, volume 35, pages 36479–36494. Curran Associates, Inc., 2022.
- [8] Aditya Ramesh, Prafulla Dhariwal, Alex Nichol, Casey Chu, and Mark Chen. Hierarchical text-conditional image generation with clip latents, 2022. 1
- [9] Amanpreet Singh, Ronghang Hu, Vedanuj Goswami, Guillaume Couairon, Wojciech Galuba, Marcus Rohrbach, and Douwe Kiela. Flava: A foundational language and vision alignment model. In *Proceedings of the IEEE/CVF Conference on Computer Vision and Pattern Recognition (CVPR)*, pages 15638–15650, June 2022. 1
- [10] Jean-Baptiste Alayrac, Jeff Donahue, Pauline Luc, Antoine Miech, Iain Barr, Yana Hasson, Karel Lenc, Arthur Mensch, Katherine Millican, Malcolm Reynolds, Roman Ring, Eliza Rutherford, Serkan Cabi, Tengda Han, Zhitao Gong, Sina Samangooei, Marianne Monteiro, Jacob L Menick, Sebastian Borgeaud, Andy Brock, Aida Nematzadeh, Sahand Sharifzadeh, Miłko aj Bińkowski, Ricardo Barreira, Oriol Vinyals, Andrew Zisserman, and Karén Simonyan. Flamingo: a visual language model for few-shot learning. In S. Koyejo, S. Mohamed, A. Agarwal, D. Belgrave, K. Cho, and A. Oh, editors, *Advances in Neural Information Processing Systems*, volume 35, pages 23716–23736. Curran Associates, Inc., 2022.
- [11] Haotian Liu, Chunyuan Li, Qingyang Wu, and Yong Jae Lee. Visual instruction tuning. In A. Oh, T. Naumann, A. Globerson, K. Saenko, M. Hardt, and S. Levine, editors, *Advances in Neural Information Processing Systems*, volume 36, pages 34892–34916. Curran Associates, Inc., 2023.
- [12] Matt Deitke, Christopher Clark, Sangho Lee, Rohun Tripathi, Yue Yang, Jae Sung Park, Mohammadreza Salehi, Niklas Muennighoff, Kyle Lo, Luca Soldaini, Jiasen Lu, Taira Anderson, Erin Bransom, Kiana Ehsani, Huong Ngo, Yen-Sung Chen, Ajay Patel, Mark Yatskar, Chris Callison-Burch, Andrew Head, Rose Hendrix, Favyen Bastani, Eli VanderBilt, Nathan Lambert, Yvonne Chou, Arnavi Chheda, Jenna Sparks, Sam Skjonsberg, Michael Schmitz, Aaron Sarnat, Byron Bischoff, Pete Walsh, Chris Newell, Piper Wolters, Tanmay Gupta, Kuo-Hao Zeng, Jon Borchardt, Dirk Groeneveld, Jen Dumas, Crystal Nam, Sophie Lebrecht, Caitlin Wittliff, Carissa Schoenick, Oscar Michel, Ranjay Krishna, Luca Weihs, Noah A. Smith, Hannaneh Hajishirzi, Ross Girshick, Ali Farhadi, and Aniruddha Kembhavi. Molmo and pixmo: Open weights and open data for state-of-the-art multimodal models, 2024.
- [13] Praveesh Agrawal, Szymon Antoniak, Emma Bou Hanna, Baptiste Bout, Devendra Chaplot, Jessica Chudnovsky, Diogo Costa, Baudouin De Monicault, Saurabh Garg, Theophile Gervet, Soham Ghosh, Amélie Héliou, Paul Jacob, Albert Q. Jiang, Kartik Khandelwal, Timothée Lacroix, Guillaume Lample, Diego Las Casas, Thibaut Lavril, Teven Le Scao, Andy Lo, William Marshall, Louis Martin, Arthur Mensch, Pavankumar Muddireddy, Valera Nemychnikova, Marie Pellat, Patrick Von Platen, Nikhil Raghuraman, Baptiste Rozière, Alexandre Sablayrolles, Lucile Saulnier, Romain Sauvestre, Wendy Shang, Roman Soletskyi, Lawrence Stewart, Pierre Stock, Joachim Studnia, Sandeep Subramanian, Sagar Vaze, Thomas Wang, and Sophia Yang. Pixtral 12b, 2024. 1, 2
- [14] Christoph Schuhmann, Romain Beaumont, Richard Vencu, Cade Gordon, Ross Wightman, Mehdi Cherti, Theo Coombes, Aarush Katta, Clayton Mullis, Mitchell Wortsman, Patrick Schramowski, Srivatsa Kundurthy, Katherine Crowson, Ludwig Schmidt, Robert Kaczmarczyk, and Jenia Jitsev. Laion-5b: An open large-scale dataset for training next generation image-text models, 2022. 1
- [15] Hugo Laurençon, Lucile Saulnier, Léo Tronchon, Stas Bekman, Amanpreet Singh, Anton Lozhkov, Thomas Wang, Siddharth Karamcheti, Alexander M. Rush, Douwe Kiela, Matthieu Cord, and Victor Sanh. Obelics: An open web-scale filtered dataset of interleaved image-text documents, 2023. 1
- [16] Yuying Ge, Sijie Zhao, Ziyun Zeng, Yixiao Ge, Chen Li, Xintao Wang, and Ying Shan. Making LLaMA SEE and draw with SEED tokenizer. In *The Twelfth International Conference on Learning Representations*, 2024. 1
- [17] Zineng Tang, Ziyi Yang, Chenguang Zhu, Michael Zeng, and Mohit Bansal. Any-to-any generation via composable diffusion. In A. Oh, T. Naumann, A. Globerson, K. Saenko, M. Hardt, and S. Levine, editors, *Advances in Neural Information Processing Systems*, volume 36, pages 16083–16099. Curran Associates, Inc., 2023. 1
- [18] Gemini Team. Gemini: A family of highly capable multimodal models, 2024.
- [19] Jun Zhan, Junqi Dai, Jiasheng Ye, Yunhua Zhou, Dong Zhang, Zhigeng Liu, Xin Zhang, Ruibin Yuan, Ge Zhang, Linyang Li, Hang Yan, Jie Fu, Tao Gui, Tianxiang Sun, Yu-Gang Jiang, and Xipeng Qiu. AnyGPT: Unified multimodal LLM with discrete sequence modeling. In Lun-Wei Ku, Andre Martins, and Vivek Srikumar, editors, *Proceedings of the 62nd Annual Meeting of the Association for Computational Linguistics (Volume 1: Long Papers)*, pages 9637–9662, Bangkok, Thailand, August 2024. Association for Computational Linguistics. 1
- [20] Chameleon Team. Chameleon: Mixed-modal early-fusion foundation models. *arXiv preprint arXiv:2405.09818*, 2024. 1, 2
- [21] Runpei Dong, Chunrui Han, Yuang Peng, Zekun Qi, Zheng Ge, Jinrong Yang, Liang Zhao, Jianjian Sun, Hongyu Zhou, Haoran Wei, Xiangwen Kong, Xiangyu Zhang, Kaisheng Ma, and Li Yi. DreamLLM: Synergistic multimodal comprehension and creation. In *The Twelfth International Conference on Learning Representations*, 2024. 1
- [22] Hong Chen, Xin Wang, Yuwei Zhou, Bin Huang, Yipeng Zhang, Wei Feng, Houjun Chen, Zeyang Zhang, Siao Tang,

- and Wenwu Zhu. Multi-modal generative ai: Multi-modal llm, diffusion and beyond, 2024. 1
- [23] Shenghao Xie, Wenqiang Zu, Mingyang Zhao, Duo Su, Shilong Liu, Ruohua Shi, Guoqi Li, Shanghang Zhang, and Lei Ma. Towards unifying understanding and generation in the era of vision foundation models: A survey from the autoregression perspective, 2024. 1
- [24] Shengqiong Wu, Hao Fei, Leigang Qu, Wei Ji, and Tat-Seng Chua. NExt-GPT: Any-to-any multimodal LLM. In *Forty-first International Conference on Machine Learning*, 2024. 1
- [25] Quan Sun, Qiyang Yu, Yufeng Cui, Fan Zhang, Xiaosong Zhang, Yueze Wang, Hongcheng Gao, Jingjing Liu, Tiejun Huang, and Xinlong Wang. Emu: Generative pretraining in multimodality. In *The Twelfth International Conference on Learning Representations*, 2024. 1
- [26] Xinlong Wang, Xiaosong Zhang, Zhengxiong Luo, Quan Sun, Yufeng Cui, Jinsheng Wang, Fan Zhang, Yueze Wang, Zhen Li, Qiyang Yu, Yingli Zhao, Yulong Ao, Xuebin Min, Tao Li, Boya Wu, Bo Zhao, Bowen Zhang, Liangdong Wang, Guang Liu, Zheqi He, Xi Yang, Jingjing Liu, Yonghua Lin, Tiejun Huang, and Zhongyuan Wang. Emu3: Next-token prediction is all you need, 2024. 1
- [27] Clement Neo, Luke Ong, Philip Torr, Mor Geva, David Krueger, and Fazl Barez. Towards interpreting visual information processing in vision-language models, 2024. 1, 2, 9
- [28] Samyadeep Basu, Martin Grayson, Cecily Morrison, Besmira Nushi, Soheil Feizi, and Daniela Massiceti. Understanding information storage and transfer in multi-modal large language models. In *The Thirty-eighth Annual Conference on Neural Information Processing Systems*, 2024. 2, 9
- [29] Yuxin Wen, Qingqing Cao, Qichen Fu, Sachin Mehta, and Mahyar Najibi. Efficient vision-language models by summarizing visual tokens into compact registers, 2024. 2
- [30] Matthew Trager, Pramuditha Perera, Luca Zancato, Alessandro Achille, Parminder Bhatia, and Stefano Soatto. Linear spaces of meanings: Compositional structures in vision-language models. In *ICCV*, pages 15349–15358, 2023. 1
- [31] Mikhail S. Burtsev, Yuri Kuratov, Anton Peganov, and Grigory V. Sapunov. Memory transformer, 2021. 2
- [32] Timothée Darcet, Maxime Oquab, Julien Mairal, and Piotr Bojanowski. Vision transformers need registers. In *The Twelfth International Conference on Learning Representations*, 2024. 2
- [33] Liang Chen, Haozhe Zhao, Tianyu Liu, Shuai Bai, Junyang Lin, Chang Zhou, and Baobao Chang. An image is worth 1/2 tokens after layer 2: Plug-and-play inference acceleration for large vision-language models, 2024. 2
- [34] David M. Chan, Rodolfo Corona, Joonyong Park, Cheol Jun Cho, Yutong Bai, and Trevor Darrell. Analyzing the language of visual tokens, 2024. 2
- [35] Ashish Vaswani, Noam Shazeer, Niki Parmar, Jakob Uszkoreit, Llion Jones, Aidan N. Gomez, Lukasz Kaiser, and Illia Polosukhin. Attention is all you need. In Isabelle Guyon, Ulrike von Luxburg, Samy Bengio, Hanna M. Wallach, Rob Fergus, S. V. N. Vishwanathan, and Roman Garnett, editors, *Advances in Neural Information Processing Systems 30: Annual Conference on Neural Information Processing Systems 2017, December 4-9, 2017, Long Beach, CA, USA*, pages 5998–6008, 2017. 3
- [36] Nelson Elhage, Neel Nanda, Catherine Olsson, Tom Henighan, Nicholas Joseph, Ben Mann, Amanda Askell, Yuntao Bai, Anna Chen, Tom Conerly, Nova DasSarma, Dawn Drain, Deep Ganguli, Zac Hatfield-Dodds, Danny Hernandez, Andy Jones, Jackson Kernion, Liane Lovitt, Kamal Ndousse, Dario Amodei, Tom Brown, Jack Clark, Jared Kaplan, Sam McCandlish, and Chris Olah. A mathematical framework for transformer circuits. *Transformer Circuits Thread*, 2021. <https://transformer-circuits.pub/2021/framework/index.html>. 3
- [37] Aaron Van Den Oord, Oriol Vinyals, et al. Neural discrete representation learning. *Advances in neural information processing systems*, 30, 2017. 3
- [38] Oran Gafni, Adam Polyak, Oron Ashual, Shelly Sheynin, Devi Parikh, and Yaniv Taigman. Make-a-scene: Scene-based text-to-image generation with human priors. In Shai Avidan, Gabriel Brostow, Moustapha Cissé, Giovanni Maria Farinella, and Tal Hassner, editors, *Computer Vision – ECCV 2022*, pages 89–106, Cham, 2022. Springer Nature Switzerland. 3
- [39] Hugo Touvron, Louis Martin, Kevin Stone, Peter Albert, Amjad Almahairi, Yasmine Babaei, Nikolay Bashlykov, Soumya Batra, Prajjwal Bhargava, Shruti Bhosale, et al. Llama 2: Open foundation and fine-tuned chat models. *arXiv preprint arXiv:2307.09288*, 2023. 3
- [40] Mistral nemo. <https://mistral.ai/news/mistral-nemo/>. Accessed: 2024-11-10. 3
- [41] Diego Doimo, Aldo Glielmo, Alessio Ansuini, and Alessandro Laio. Hierarchical nucleation in deep neural networks. *Advances in Neural Information Processing Systems*, 33, 2020. 3
- [42] Mor Geva, Jasmijn Bastings, Katja Filippova, and Amir Globerson. Dissecting recall of factual associations in autoregressive language models. In Houda Bouamor, Juan Pino, and Kalika Bali, editors, *Proceedings of the 2023 Conference on Empirical Methods in Natural Language Processing, EMNLP 2023, Singapore, December 6-10, 2023*, pages 12216–12235. Association for Computational Linguistics, 2023. 4
- [43] Atticus Geiger, Hanson Lu, Thomas Icard, and Christopher Potts. Causal abstractions of neural networks. In Marc’Aurelio Ranzato, Alina Beygelzimer, Yann N. Dauphin, Percy Liang, and Jennifer Wortman Vaughan, editors, *Advances in Neural Information Processing Systems 34: Annual Conference on Neural Information Processing Systems 2021, NeurIPS 2021, December 6-14, 2021, virtual*, pages 9574–9586, 2021. 4
- [44] Arthur Conmy, Augustine N. Mavor-Parker, Aengus Lynch, Stefan Heimersheim, and Adrià Garriga-Alonso. Towards automated circuit discovery for mechanistic interpretability. In Alice Oh, Tristan Naumann, Amir Globerson, Kate Saenko, Moritz Hardt, and Sergey Levine, editors, *Advances in Neural Information Processing Systems 36: Annual Conference on Neural Information Processing Systems 2023, NeurIPS 2023, New Orleans, LA, USA, December 10 - 16, 2023*, 2023. 4

- [45] Paul Jaccard. Distribution de la flore alpine dans le bassin des dranses et dans quelques régions voisines. *Bull Soc Vaudoise Sci Nat*, 37:241–272, 1901. 4
- [46] Facebook AI. Chameleon-7b. <https://huggingface.co/facebook/chameleon-7b>, 2024. 4
- [47] Facebook AI. Chameleon-30b. <https://huggingface.co/facebook/chameleon-30b>, 2024. 4
- [48] Mistral Community. Pixtral-12b. <https://huggingface.co/mistral-community/pixtral-12b>, 2024. 4
- [49] Peter Young, Alice Lai, Micah Hodosh, and Julia Hockenmaier. From image descriptions to visual denotations: New similarity metrics for semantic inference over event descriptions. *Transactions of the Association for Computational Linguistics*, 2:67–78, 2014. 4, 7, 1, 3
- [50] Maria d’Errico, Elena Facco, Alessandro Laio, and Alex Rodriguez. Automatic topography of high-dimensional data sets by non-parametric density peak clustering. *Information Sciences*, 560:476–492, 2021. 5, 1
- [51] Andrew Rosenberg and Julia Hirschberg. V-measure: A conditional entropy-based external cluster evaluation measure. In Jason Eisner, editor, *Proceedings of the 2007 Joint Conference on Empirical Methods in Natural Language Processing and Computational Natural Language Learning (EMNLP-CoNLL)*, pages 410–420, Prague, Czech Republic, June 2007. Association for Computational Linguistics. 5
- [52] Olga Russakovsky, Jia Deng, Hao Su, Jonathan Krause, Sanjeev Satheesh, Sean Ma, Zhiheng Huang, Andrej Karpathy, Aditya Khosla, Michael Bernstein, et al. Imagenet large scale visual recognition challenge. *International journal of computer vision*, 115:211–252, 2015. 5
- [53] Yash Goyal, Tejas Khot, Douglas Summers-Stay, Dhruv Batra, and Devi Parikh. Making the V in VQA matter: Elevating the role of image understanding in Visual Question Answering. In *Conference on Computer Vision and Pattern Recognition (CVPR)*, 2017. 7
- [54] Tsung-Yi Lin, Michael Maire, Serge Belongie, James Hays, Pietro Perona, Deva Ramanan, Piotr Dollár, and C. Lawrence Zitnick. Microsoft coco: Common objects in context. In David Fleet, Tomas Pajdla, Bernt Schiele, and Tinne Tuytelaars, editors, *Computer Vision – ECCV 2014*, pages 740–755, Cham, 2014. Springer International Publishing. 7, 3
- [55] Emily Cheng, Diego Doimo, Corentin Kervadec, Iuri Maccocco, Jade Yu, Alessandro Laio, and Marco Baroni. Emergence of a high-dimensional abstraction phase in language transformers. *arXiv preprint arXiv:2405.15471*, 2024. 1
- [56] Diego Doimo, Alessandro Serra, Alessio Ansuini, and Alberto Cazzaniga. The representation landscape of few-shot learning and fine-tuning in large language models, 2024. 1
- [57] Stanislaw Antol, Aishwarya Agrawal, Jiasen Lu, Margaret Mitchell, Dhruv Batra, C. Lawrence Zitnick, and Devi Parikh. Vqa: Visual question answering. In *Proceedings of the IEEE International Conference on Computer Vision (ICCV)*, December 2015. 2
- [58] Ramakrishna Vedantam, C Lawrence Zitnick, and Devi Parikh. Cider: Consensus-based image description evaluation. In *Proceedings of the IEEE conference on computer vision and pattern recognition*, pages 4566–4575, 2015. 3

The Narrow Gate: Localized Image-Text Communication in Vision-Language Models

Supplementary Material

7. Advanced density peaks clustering.

The Advanced Density Peaks (ADP) clustering [50] is a mode-seeking, density-based clustering algorithm that finds the modes of the probability density on the data’s low-dimensional data without performing any explicit dimensional reduction. We summarize the main steps below and refer the interested reader to the original paper [50].

The algorithm consists of three steps: the estimation of the data’s intrinsic dimension, the estimation of the local density around each point, and a final density-based clustering of the data. Following previous works [55, 56], we estimate the intrinsic dimension with `GridE`, a neighbor-based intrinsic dimension estimator, setting the rank k of the nearest neighbor involved in the estimate to 16 (see [56] for more details). We then measure the local density around each data point with a k NN approach: $\rho_{i,k} = \frac{k}{NV_k}$. Here, N is the number of data points, and V is the volume of the ball, which has a radius equal to the distance between the point i and its k^{th} nearest neighbor. Importantly, we measure the volume on the intrinsic manifold using the intrinsic dimension value estimated in the first step.

The third step is the density-based clustering. With the knowledge of the ρ_i , we find a collection of density peaks $\mathcal{C} = \{c^1, \dots, c^n\}$, assign the data points around them, and find the density $\rho^{\alpha,\beta}$ of saddle points between a pair of clusters c_α c_β with the procedure described in [50]. The statistical reliability of the peaks is assessed with a t -test on $\log \rho^\alpha - \log \rho^{\alpha,\beta}$, where ρ^α is the maximum density of peak c_α , and $\rho^{\alpha,\beta}$ the density of the saddle point between c_α and c_β . Once the confidence level Z is fixed, all the clusters that do not pass the t -test are merged since the value of their density peaks are considered indistinguishable from the nearby saddle point. The process is repeated until all the peaks satisfy the t -test and are statistically robust with a confidence Z [50].

In the analysis reported in Sec. 4.1 we remove clusters with size lower than 50.

8. Experimental Setup

8.1. Image-text prompt constructed from Flickr-30k

The Flickr-30k [49] dataset comprises 30,000 images, each associated with five captions. To generate prompts that alternate between text-first and image-first formats, we structured the inputs by concatenating all five captions for each image, either preceding or following the image itself, depending on

the intended sequence.

8.2. Image-text prompt constructed from ImageNet

For all experiments involving ImageNet images, we use a consistent subset of the dataset. We randomly select 100 animal classes and sample 100 images from each class, yielding 10,000 images. The selected classes are:

- `staffordshire_bullterrier.n.01`
- `otterhound.n.01`
- `appenzeller.n.01`
- `chow.n.03`
- `hornbill.n.01`
- `basenji.n.01`
- `australian_terrier.n.01`
- `chesapeake_bay_retriever.n.01`
- `irish_setter.n.01`
- `scotch_terrier.n.01`
- `red_wolf.n.01`
- `american_staffordshire_terrier.n.01`
- `labrador_retriever.n.01`
- `standard_poodle.n.01`
- `lakeland_terrier.n.01`
- `saluki.n.01`
- `thunder_snake.n.01`
- `platypus.n.01`
- `dragonfly.n.01`
- `rhodesian_ridgeback.n.01`
- `spiny_lobster.n.02`
- `chambered_nautilus.n.01`
- `komondor.n.01`
- `collie.n.01`
- `egyptian_cat.n.01`
- `leonberg.n.01`
- `vizsla.n.01`
- `flat_coated_retriever.n.01`
- `fiddler_crab.n.01`
- `eskimo_dog.n.01`
- `affenpinscher.n.01`
- `boston_bull.n.01`
- `samoyed.n.03`
- `dungeness_crab.n.02`
- `french_bulldog.n.01`
- `groenendael.n.01`
- `bee_eater.n.01`
- `snow_leopard.n.01`
- `toy_terrier.n.01`
- `killer_whale.n.01`

- entlebucher.n.01
- spotted_salamander.n.01
- mexican_hairless.n.01
- chihuahua.n.03
- ruffed_grouse.n.01
- giant_schnauzer.n.01
- brittany_spaniel.n.01
- brabancon_griffon.n.01
- pekinese.n.01
- cocker_spaniel.n.01
- loggerhead.n.02
- pembroke.n.01
- agama.n.01
- black_and_gold_garden_spider.n.01
- ostrich.n.02
- sealyham_terrier.n.01
- bernese_mountain_dog.n.01
- maltese_dog.n.01
- black_and_tan_coonhound.n.01
- redbone.n.01
- spider_monkey.n.01
- welsh_springer_spaniel.n.01
- admiral.n.02
- komodo_dragon.n.01
- borzoi.n.01
- briard.n.01
- bluetick.n.01
- norwegian_elkhound.n.01
- macaw.n.01
- great_dane.n.01
- greater_swiss_mountain_dog.n.01
- hermit_crab.n.01
- tailed_frog.n.01
- tench.n.01
- bloodhound.n.01
- german_short-haired_pointer.n.01
- tree_frog.n.02
- soft-coated_wheaten_terrier.n.01
- green_lizard.n.01
- alligator_lizard.n.01
- ringneck_snake.n.01
- persian_cat.n.01
- sidewinder.n.01
- italian_greyhound.n.01
- bedlington_terrier.n.01
- puffer.n.02
- bull_mastiff.n.01
- miniature_pinscher.n.01
- shetland_sheepdog.n.01
- red-breasted_merganser.n.01
- beagle.n.01
- banded_gecko.n.01
- white_wolf.n.01

- african_elephant.n.01
- arabian_camel.n.01
- indigo_bunting.n.01
- miniature_schnauzer.n.01
- irish_terrier.n.01
- peacock.n.02
- kelpie.n.02

For the activation patching experiment, described in Sec. 4.4, we manually select 20 class from the list above to ensure semantic diversity in the animal represented, and then we random sample 100 images for each class, obtaining a total of 2000 images. The selected pairs are:

- (american_alligator.n.01, arabian_camel.n.01)
- (bald_eagle.n.01, barn_spider.n.01)
- (bee_eater.n.01, cheetah.n.01)
- (flamingo.n.01, great_grey_owl.n.01)
- (green_mamba.n.01, grey_whale.n.01)
- (hippopotamus.n.01, jaguar.n.01)
- (king_penguin.n.01, kit_fox.n.01)
- (lionfish.n.01, macaw.n.01)
- (proboscis_monkey.n.01, siberian_husky.n.01)
- (tailed_frog.n.01, trilobite.n.01)

Then for the experiment described in Sec. 4.2, Sec. 4.3 we use the following prompt construction “<image> This animal is a”. For the activation patching experiment described in Sec. 4.4 we use the same prompt for Chameleon-7B. For Chameleon-34B, we adopt a slightly modified prompt: “<image> Answer the question using a single word, number, or short phrase. This animal is a” as Chameleon-34B refused to respond to the original prompt.

8.3. Metrics

VQA accuracy. The Visual Question Answering (VQA) [57] benchmark relies on annotations provided by 10 Amazon Mechanical Turk workers for each image-question pair, with the most frequently given answer designated as the ground truth. The evaluation metric, denoted as $\text{Acc}(\text{ans})$, is defined as follows:

$$\text{Acc}(\text{ans}) = \min \left\{ \frac{\#\text{humans that said ans}}{3}, 1 \right\}.$$

This formulation ensures robustness by weighting answers based on consensus among annotators, capping the contribution of an answer to the accuracy score at 1.0. Before evaluating the answers provided by the models, both ground truth and predicted answers are preprocessed to standardize formatting and mitigate discrepancies arising from superficial variations; for further information, we refer to the

VQA evaluation script ². These steps include:

1. **Lowercasing:** All characters are converted to lowercase.
2. **Period Handling:** Periods are removed unless they appear in decimal numbers.
3. **Numerical Normalization:** Number words are converted to digits.
4. **Article Removal:** Articles (“a,” ”an,” ”the”) are omitted.
5. **Contraction Normalization:** Missing apostrophes in contractions are restored (e.g., “dont” becomes “don’t”).
6. **Punctuation Handling:**
 - Most punctuation marks are replaced with a space, except apostrophes and colons.
 - Apostrophes are preserved to avoid altering possessive forms.
 - Colons are retained for time-related references.
 - Commas between digits are removed without inserting spaces (e.g., “100,978” becomes “100978”).

CIDEr For the captioning benchmarks on Flickr [49] and MS COCO [54], we used CIDEr [58] metric. This metric assesses the quality of image captions by comparing a candidate sentence c_i to a set of reference sentences $\mathcal{R}_i = \{\mathbf{r}_{i1}, \dots, \mathbf{r}_{im}\}$ associated with an image I_i . The CIDEr metric evaluates candidate sentences by representing both the candidate and reference sentences as n -grams, which are sequences of 1-4 words reduced to their root forms (e.g., “fishing,” “fished,” and “fishes” become “fish”). To measure their relevance, a Term Frequency-Inverse Document Frequency (TF-IDF) weighting is employed where Term Frequency (TF) captures the frequency of an n -gram ω_k within a sentence, and Inverse Document Frequency (IDF) discounts n -grams that are common across the dataset, for the explicit formula we refer to the original paper [58]

Using these weights, the metric calculates the cosine similarity between the TF-IDF-weighted n -gram vectors of the candidate sentence and the reference sentences, capturing their alignment. This similarity is expressed as:

$$\text{CIDEr}_n(c_i, \mathcal{R}_i) = \frac{1}{m} \sum_j \frac{\mathbf{g}^n(c_i) \cdot \mathbf{g}^n(\mathbf{r}_{ij})}{\|\mathbf{g}^n(c_i)\| \|\mathbf{g}^n(\mathbf{r}_{ij})\|},$$

where \mathbf{g}^n represents the TF-IDF-weighted vector for n -grams. The CIDEr score aggregates these similarity scores across n -grams of different lengths, combining them with equal weights for $n \in \{1, 2, 3, 4\}$ as follows:

$$\text{CIDEr}(c_i, \mathcal{R}_i) = \frac{1}{4} \sum_{n=1}^4 \text{CIDEr}_n(c_i, \mathcal{R}_i).$$

²<https://github.com/GT-Vision-Lab/VQA/tree/master>

9. Additional Results for Cross-Modal Attention

The results for Chameleon-34B closely align with those observed for Chameleon-7B described in Sec. 4.2. The three tokens—[EOI], the first image token, and the last—dominate cross-modal attention. As seen in Chameleon-7B, only [EOI] consistently exhibits high $\chi^{l,gt}$ values from the early layers through to the final ones. In contrast, all other tokens maintain consistently low overlap values, near zero, indicating that these positions contribute minimally to encoding meaningful visual information from the image.

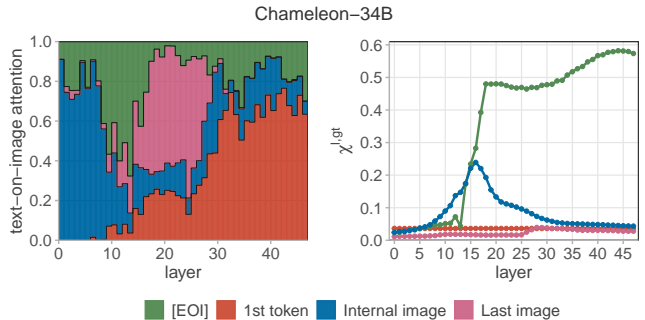


Figure A1. **Localization of information in Chameleon-34B** (left) Contribution of different image token positions to the total text-on-image attention across layers. Tokens with an average contribution larger than 1% are shown individually. The remaining tokens are aggregated as “internal image”. (right) Neighborhood overlap between selected image tokens and ImageNet labels The blue curve is obtained by averaging over all internal image tokens excluding the first one.

10. Additional Results for Ablation

Table A2 extends the results of Table 1, showing the ablation effect on all tokens identified for their high cross-modal attention. The analysis further confirms that none of the special tokens, except for [EOI], play a significant role, as their ablation does not noticeably affect performance across the benchmarks.

11. Additional Results for Activation Patching

In Fig. A2, we show an additional experiment on patching that complements the picture depicted in Sec. 4.4.

Model	Ablation	VQAv2	Flickr	MS-COCO	ImageNet ($\chi^{out,gt}$)
Chameleon-7B	-	0.51	0.23	0.35	0.46
	[EOI]	0.25	0.04	0.03	0.01
	Last-Image	0.42	0.17	0.25	0.46
	32nd	0.51	0.23	0.34	0.46
	Random	0.51	0.21	0.31	0.46
Chameleon-34B	-	0.59	0.38	0.42	0.43
	[EOI]	0.39	0.02	0.02	0.04
	Last-Image	0.58	0.35	0.40	0.41
	First-Image	0.57	0.35	0.39	0.42
	Random	0.58	0.34	0.38	0.42
Pixtral	-	0.79	0.51	0.60	0.63
	[EOI]	0.77	0.53	0.58	0.61
	Last-Image	0.77	0.49	0.59	0.62
	1025	0.77	0.46	0.55	0.61
	[EOL]s	0.76	0.46	0.54	0.61
	Random	0.77	0.46	0.55	0.61

Table A2. **Effect of Attention Knockout on Image Understanding Tasks.** Performance of Chameleon (7B and 34B) and Pixtral models on visual question answering (VQAv2), image captioning (Flickr-30k and MS-COCO), and image classification (ImageNet) under different attention ablation settings. Depending on the model, we ablated the special tokens with high cross-modality attention by removing their communication with the text tokens. The “Random” baseline represents the average performance after ablating ten randomly selected image tokens, repeated 10 times. Since the standard deviation was consistently < 0.02 we omitted it

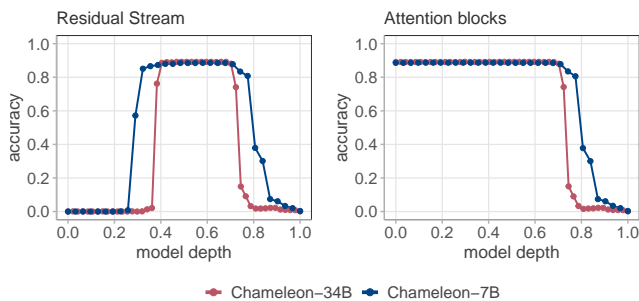


Figure A2. **Layer-wise Accuracy After Activation Patching at [EOI] in Chameleon Models.** Impact of activation patching on model predictions by quantifying the frequency at which the model switches from predicting the base class to the target class. **(left)** Direct residual stream patching, where activations from a target image replace those of a base image at individual layers, with the y-axis showing the proportion of cases where the model adopts the target image’s classification. **(right)** Cumulative attention patching, where we replace all attention vectors at the [EOI] position from a specified depth onward.